Parametric study of a vibro-impact wave energy converter

Bingyong Guo [*] **John V. Ringwood** [*]

[*] *Centre for Ocean Energy Research, Department of Electronic Engineering, Maynooth University, Maynooth, Ireland, (e-mail:Bingyong.Guo@mu.ie; John.Ringwood@mu.ie)*

Abstract: In this study, a non-linear vibro-impact mechanism is integrated inside a semi-submerged cylindrical heaving point absorber in order to enhance its power capture by utilising the non-linearity of vibro-impact events. A piece-wise linear model is derived considering linear wave-buoy interaction and the non-linear vibro-impact mechanism. Since the dynamics and performance of the vibro-impact wave energy converter (WEC) are sensitive to design parameters, a parametric study and analysis are conducted numerically by varying the design parameters in a broad range to evaluate their influence on the vibro-impact WEC's dynamics and performance, in terms of response amplitude operator, average power output and peak-to-average power ratio. Numerical simulations show that there exist some optimal sets of the design parameters to achieve a trade-off among the aforementioned performance indices. Hence, the parametric study in this paper can give some basic guidelines for optimising and prototyping the design of the vibro-impact WEC for wave tank testing.

Keywords: Wave Energy Conversion, Heaving Point Absorber, Vibro-Impact Mechanism, Non-linear Power Take-Off, Parametric Study.

1. INTRODUCTION

To harvest energy from ocean waves, various technologies and devices have been examined (Drew et al., 2009; Falcão, 2010; Babarit et al., 2012). These wave energy converters (WECs) can be classified into the following five predominant types: oscillating water columns, attenuators, point absorbers (PAs), terminators, and over-topping devices. Among the aforementioned WECs, the heaving PA may be one of the simplest and most promising concepts (Ricci et al., 2009), since it is easy to install and economical to maintain. PAs can be categorised into three subtypes, including (i) one-body PAs, e.g. the CETO buoy, (ii) two-body PAs, e.g. the Wavebob buoy and the OPT's PowerBuoy, and (iii) PA arrays, e.g. the WaveStar device.

These PAs can harvest energy efficiently when resonance occurs. However, PAs' resonance bandwidths are narrow, while wave spectra are generally broader. One way to maximise power absorption of WECs across a wide frequency range is to utilise control approaches (Ringwood et al., 2014). Another way is to design novel WEC concepts or power take-off (PTO) systems. Some non-linear PTO concepts have the potential to improve power capture width and to widen resonance bandwidth. For example, Bailey (2010) investigated the influence of non-linear PTO dampers on WECs' power capture by numerical and experimental testing. In addition to non-linear dampers, Zhang
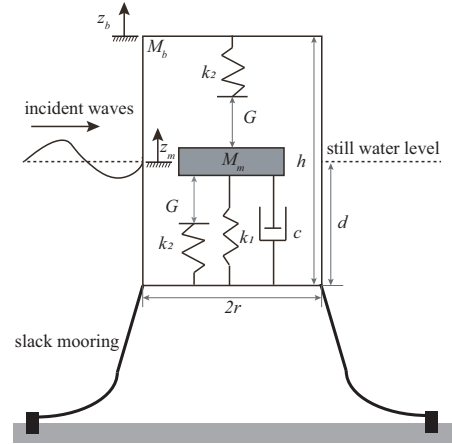
Fig. 1. Schematic diagram of a vibro-impact mechanism integrated inside a cylindrical heaving point absorber.

et al. (2014) proposed a bi-stable mechanical system, consisting of two symmetrically oblique springs, to achieve negative stiffness by a snap-through mechanism. Based on the same principle, CorPower Ocean invented a 'negative' spring, termed WaveSpring, to increase WECs' response bandwidth (Todalshaug et al., 2016). These studies conclude that a properly designed non-linear PTO system has the potential to maximise power absorption over a wide range of wave frequencies. As resonance is achieved by control or novel PTO design, PAs' heaving motion may be large enough to violate physical constraints (Chen et al., 2017). Therefore, an end-stop function is required, and can be achieved by mechanical design or optimal control considering physical constraints (Zhan and Li, 2018).

This study proposes a vibro-impact WEC which uses a non-linear vibro-impact mechanism to enhance power capture, to broaden its bandwidth and to provide an end-stop function. As shown in Fig. 1, a semi-submerged cylindrical buoy (M_b) is excited by incident waves, and oscillates as a result. An inner mass (M_m) is connected to the buoy by a linear PTO damper (c) and a supporting spring (k_1), and oscillates accordingly due to the interaction force with the buoy. The supporting spring is prestressed to balance the inner mass at its equilibrium point with a suitable original length. The key mechanism is that the upper and lower impact springs (k_2), attached to the top and floor of the buoy, induce vibro-impact events when the relative displacement between the inner mass and buoy exceeds the upper or lower gaps (G). The non-linear vibro-impact events increase the WEC's complexity, but have the potential to improve the WEC's power capture bandwidth.

End-stop springs were previously used to limit heave motion of PAs (Jaya Muliawan et al., 2013; Göteman et al., 2015; Chen et al., 2017). However, the effect of end-stop setups under a wide range of variation in design parameters, including M_m, k_1, k_2, G and c, on PAs' dynamics and power capture is missing. As a preliminary study of the modelling of the vibro-impact WEC in Fig. 1 was discussed by Guo and Ringwood (2020), with specific focuses on the vibro-impact induced non-linear dynamics, end-stop performance and comparison with normal WEC without vibro-impact, this paper only focuses on a numerical parametric study to emphasise how the design parameters influence the vibro-impact WEC's dynamics and power absorption under regular wave conditions. Numerical simulations demonstrate that: (i) The response amplitude operator (RAO) of the relative motion between the inner mass and the buoy acts like a "band-pass filter", with relatively small gain value when the wave frequency is low. (ii) The dynamics and power capture of the vibro-impact WEC are sensitive to the design parameters. Hence, the system performance, in terms of relative RAO and average power output, can be optimised by adjusting M_m, k_1, k_2, G and c. (iii) Occurrence of impacts may increase the peak-to-average power ratio of the PTO under certain settings, but the peak-to-average power ratio can be constrained, even reduced under certain sets of design parameters.

The remainder of the paper is organised as follows: Section 2 details the wave-buoy interaction, while the vibro-impact mechanism is detailed in Section 3. Section 4 discusses the parametric study to investigate how the design parameters influence the dynamics and performance of the vibro-impact WEC. Some concluding remarks are drawn up in Section 5.

2. WAVE-BUOY INTERACTION

As shown in Fig. 1, a cylindrical buoy is considered, and its radius, height and draft are $r = 1$ m, $h = 2$ m, and $d = 1$ m, respectively. As this study mainly focuses on how the design parameters influence the dynamics and performance of the vibro-impact WEC, the buoy's motion is constrained to heave mode only. Therefore, the dynamics of the buoy are governed by

$$M_b \ddot{z}_b = f_e + f_r + f_{hs} + f_i, \qquad (1)$$

where f_e is the excitation force due to incident waves and diffraction, f_r is the radiation force related to the motion of the buoy, f_{hs} is the hydrostatic restoring force representing the mismatch between gravity and the device buoyancy, and f_i represents the interaction force between the inner mass and the buoy. M_b, z_b and $\ddot{z}_b$ are the buoy mass, heave displacement and acceleration, respectively.

For the buoy in Fig. 1, the hydrostatic force is given as

$$f_{hs} = -\rho g \pi r^2 z_b, \qquad (2)$$

where ρ and g are the water density and gravity constant, respectively. The radiation force, in the time-domain, is written as the Cummins formula (Cummins, 1962), as

$$f_r = -m_\infty \ddot{z}_b - k_r * \dot{z}_b, \qquad (3)$$

where m_∞, k_r and $\dot{z}_b$ are the added mass at infinite frequency, the impulse response function (IRF) of the radiation force, and the velocity of the buoy in heave, respectively. The symbol $*$ represents the convolution operator. The hydrodynamic coefficients are computed using the boundary element method code NEMOH (Babarit and Delhommeau, 2015), and the radiation IRF is shown in Fig. 2(a). The convolution term of the radiation force in Eq. (3), $f_{rc} = k_r * \dot{z}_b$, can be approximated by a finite order state-space model (Guo et al., 2017b; Faedo et al., 2018), written as

$$\dot{x}_r = A_r x_r + B_r \dot{z}_b, \qquad (4)$$
$$f_{rc} \approx C_r x_r, \qquad (5)$$

where $x_r \in \mathbb{R}^{n \times 1}$ is the state vector for the identified system. $A_r \in \mathbb{R}^{n \times n}$, $B_r \in \mathbb{R}^{n \times 1}$, $C_r \in \mathbb{R}^{1 \times n}$ are the system matrices given in the Appendix. n is the dynamical order which is selected by trial and error via evaluating the goodness of fit, defined by the normalised mean square-error (Guo et al., 2017b). In this study, $n = 4$ is used, and the goodness of fit is 0.9998.

The excitation force can be determined by its frequency response function (FRF), as

$$F_e(j\omega) = H_e(j\omega)A(j\omega), \qquad (6)$$

where $H_e(j\omega)$ is the FRF of the excitation force and $A(j\omega)$ is the frequency-domain representation of incident wave $\eta(t)$. In Fig. 2(b), the excitation FRF is represented by its amplitude response $|H_e(j\omega)|$ and phase response $\angle H_e(j\omega)$. Alternatively, the excitation force can be rewritten in the time-domain as

$$f_e(t) = k_e(t) * \eta(t) = \int_{-\infty}^{\infty} k_e(t - \tau)\eta(\tau)d\tau, \qquad (7)$$

where $k_e(t) = \frac{1}{2\pi} \int_{-\infty}^{\infty} H_e(j\omega)e^{j\omega t}d\omega$ is the excitation force IRF. Based on the excitation FRF in Fig. 2(b), the excitation IRF $k_e(t)$ is represented by the black dash-dot curve in Fig. 2(c). However, $k_e(t)$ is non-causal since $k_e(t) \neq 0$ for $t < 0$ (see the shadowed area in Fig. 2(c)). The physical explanation of the non-causality is discussed by Falnes (2002).

Causalisation and approximation of the excitation were studied by Guo et al. (2017a, 2018), in which a time-shifting technique was applied to causalise the non-causal kernel function $k_e(t)$ to its causalised form $k_{e,c}(t)$ with causalisation time t_c ($t_c \geq 0$). Thus, wave prediction with a horizon of t_c is required. According to the time shift property of the convolution operator, the causalised
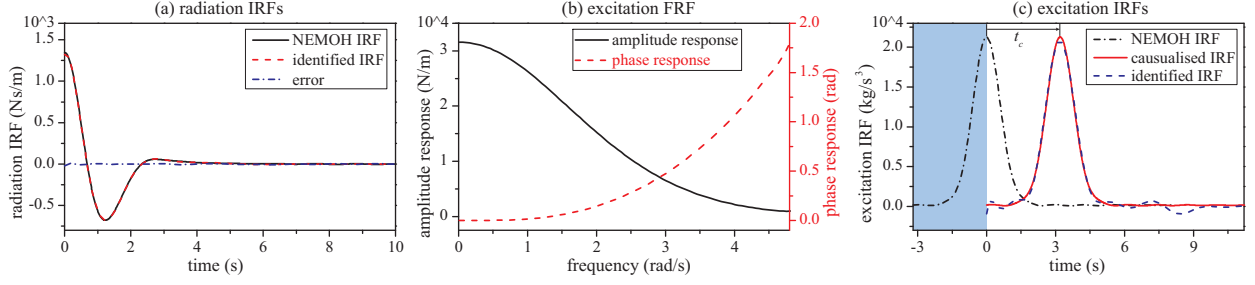
Fig. 2. (a) Radiation IRFs, (b) excitation FRF and (c) excitation IRFs. In (b), the excitation FRF is represented by its amplitude response $|H_e(j\omega)|$ and phase response $\angle H_e(j\omega)$.

system with wave prediction gives the same excitation force of the non-causal system, since

$$f_e(t) = k_e(t) * \eta(t) \tag{8}$$
$$= k_e(t + t_c) * \eta(t + t_c) = k_{e,c}(t) * \eta_p(t), \tag{9}$$

where $k_{e,c}(t) = k_e(t - t_c)$ and $\eta_p(t) = \eta(t + t_c)$ are the causalised excitation IRF (see the red solid curve in Fig. 2(c)) and the predicted wave elevation advanced by t_c, respectively. Wave prediction is required and several forecasting methods have been investigated by Fusco and Ringwood (2010).

Similarly, Eq. (9) can be approximated by a finite order state-space model, written as

$$\dot{x}_e = A_e x_e + B_e \eta_p, \tag{10}$$
$$f_e \approx C_e x_e + D_e \eta_p, \tag{11}$$

where $x_e \in \mathbb{R}^{n \times 1}$ is the state vector for the excitation system. $A_e \in \mathbb{R}^{n \times n}$, $B_e \in \mathbb{R}^{n \times 1}$, $C_e \in \mathbb{R}^{1 \times n}$ and $D_e \in \mathbb{R}^{1 \times 1}$ are the system matrices given in the Appendix, and n is the order. t_c and n are selected by trial and error via evaluating the truncation error and goodness of fit, defined by Guo et al. (2018). In this study, $t_c = 3.2$ s and $n = 6$ are selected, and the identified excitation IRF is compared with the causalised excitation IRF in Fig. 2(c) with a truncation error of less than 0.0073 and a goodness of fit of 0.9953.

3. VIBRO-IMPACT MECHANISM

For the inner mass, its equation of motion is given as

$$M_m \ddot{z}_m = -f_i, \tag{12}$$

where M_m, z_m and $\ddot{z}_m$ represent the inner mass, and its displacement and acceleration in heave, respectively. The interaction force f_i depends on the relative displacement between the inner mass and the buoy, $z_r = z_m - z_b$. As shown in Fig. 3(a), when the relative displacement is larger than or equal to the gap G, that is $z_r \geq G$, the supporting spring (k_1), the upper impact spring (k_2), and the PTO damper (c) are active. Therefore, f_i can be written as

$$f_i = k_1 z_r + k_2(z_r - G) + c v_r, \tag{13}$$

where $v_r = \dot{z}_r$ represent the relative velocity.

As shown in Fig. 3(b), when $G > z_r > -G$, the supporting spring (k_1) and the PTO damper (c) are active. Therefore, f_i can be written as

$$f_i = k_1 z_r + c v_r. \tag{14}$$

For the case $z_r \leq -G$ in Fig. 3(c), the supporting spring (k_1), the lower impact spring (k_2), and the PTO damper (c) are active. Hence, f_i can be written as
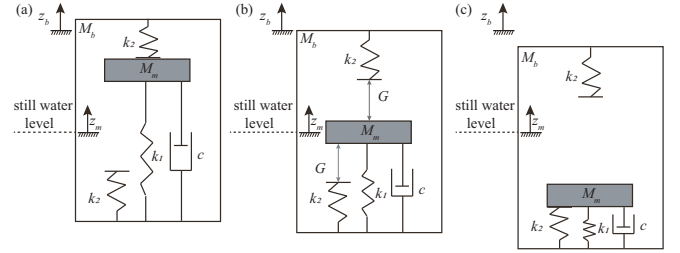

Fig. 3. Three operation modes of the vibro-impact WEC.

$$f_i = k_1 z_r + k_2(z_r + G) + c v_r. \tag{15}$$

4. PARAMETRIC STUDY

In this section, a parametric study is conducted to investigate how these parameters influence the vibro-impact WEC's performance. For clarity, regular wave condition, with wave height H and period T, is considered. To evaluate the dynamics of the vibro-impact WEC, the relative RAO is defined as

$$RAO_r = 2\max(z_r)/H, \tag{16}$$

In this study, a pure damper is used as the PTO device. To evaluate the performance of the vibro-impact WEC, the instantaneous power P_i, average power P_a and peak-to-average power ratio P_{p2a} are defined as

$$P_i = c v_r^2, \tag{17}$$
$$P_a = \frac{1}{T} \int_0^T P_i \mathrm{d}t, \tag{18}$$
$$P_{p2a} = \max(P_i)/P_a. \tag{19}$$

4.1 Influence of Inner Mass

The influence of the inner mass on the relative RAO, average power, and peak-to-average power ratio is shown in Fig. 4. As shown in Figs. 4(a)-(b), the relative RAO and average power are characterised by a band-pass effect, where the bandwidth is sensitive to the variation in the inner mass. The bandwidth initially increases and then decrease as M_m increases from 200 kg to 3000 kg, while the resonance frequency decreases monotonically. In Fig. 4(c), the maximal and minimal values of the peak-to-average power ratio are 3.5 and 1.5, respectively. That is, the peak-to-average power ratio can be either amplified or attenuated by the vibro-impact mechanism, depending on design parameter values and wave conditions. Therefore, $M_m \in [750, 1500]$ kg is preferred to achieve a large relative
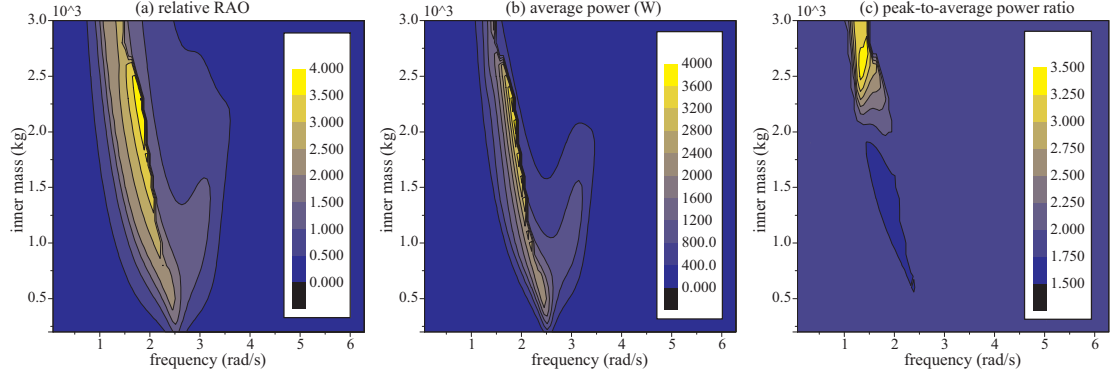
Fig. 4. (a) Relative RAO, (b) average power output, and (c) peak-to-average power ratio, with $M_m \in [200, 3000]$ kg, $\omega \in [0.06, 6.28]$ rad/s, $k_1 = 5000$ N/m, $k_2 = 20000$ N/m, $G = 0.8$ m, $c = 1000$ Ns/m, and $H = 0.8$ m.
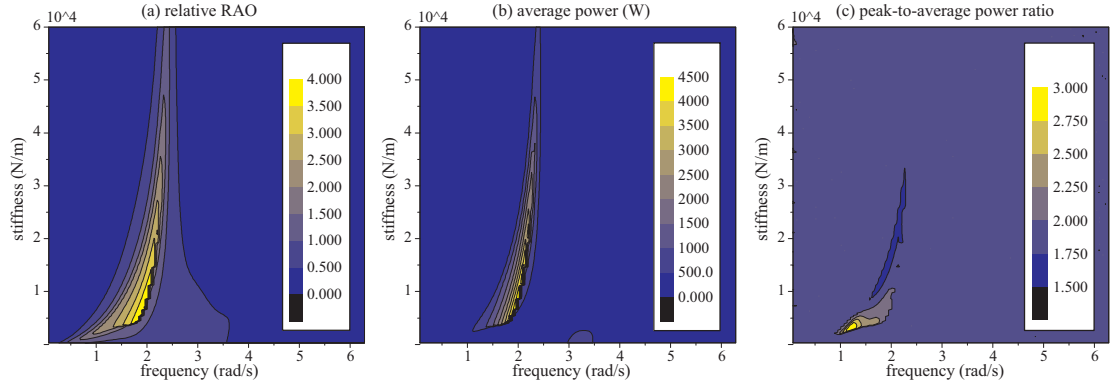

Fig. 5. (a) Relative RAO, (b) average power output, and (c) peak-to-average power ratio, with $k_1 \in [300, 60000]$ N/m, $\omega \in [0.06, 6.28]$ rad/s, $M_m = 1500$ kg, $k_2 = 20000$ N/m, $G = 0.8$ m, $c = 1000$ Ns/m, and $H = 0.8$ m.
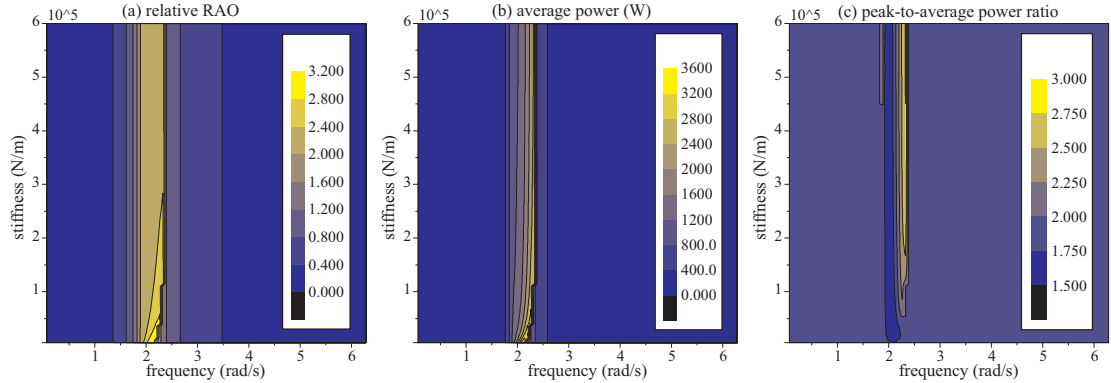

Fig. 6. (a) Relative RAO, (b) average power output, and (c) peak-to-average power ratio, with $k_2 \in [5000, 600000]$ N/m, $\omega \in [0.06, 6.28]$ rad/s, $M_m = 1500$ kg, $k_1 = 10000$ N/m, $G = 0.8$ m, $c = 1000$ Ns/m, and $H = 0.8$ m.

RAO, a high average power, a broad bandwidth, and a low peak-to-average power ratio, simultaneously.

4.2 Influence of Stiffness

By adjusting k_1, the vibro-impact WEC's dynamics and performance vary significantly, as shown in Fig. 5. As shown in Figs. 5(a)-(b), the resonance frequency increases slightly as k_1 increases, while the bandwidth of the relative RAO and average power output decreases significantly. In Fig. 5(c), the peak-to-average power ratio is low, with a maximum value of 3 and a minimum value of 1.5. $k_1 \in [5000, 20000]$ N/m is preferred for achieving a

trade-off among the relative RAO, average power, capture bandwidth, and peak-to-average power ratio.

Variation in k_2 has little influence on the dynamics and performance of the vibro-impact WEC, which is illustrated in Fig. 6. The relative RAO, average power, bandwidth and peak-to-average power ratio are robust to the change of k_2. Meanwhile, harder end-stop impact springs are preferred to limit the relative heave motion. Therefore, the suitable region is $k_2 \in [50000, 200000]$ N/m. Comparing Figs. 5 and 6, it is clear that the dynamics and performance of the vibro-impact WEC are more sensitive to the stiffness of the supporting spring than the impact springs.
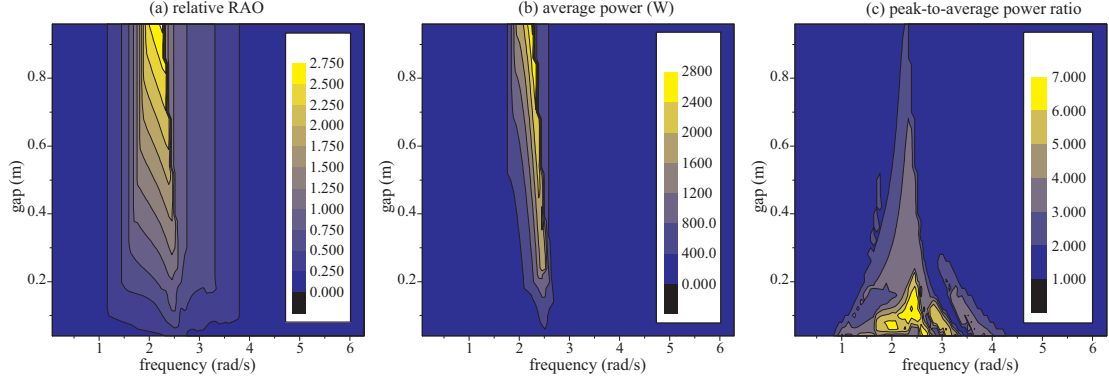
Fig. 7. (a) Relative RAO, (b) average power output, and (c) peak-to-average power ratio, with $G \in [0.04, 0.96]$ m, $\omega \in [0.06, 6.28]$ rad/s, $M_m = 1500$ kg, $k_1 = 10000$ N/m, $k_2 = 200000$ N/m, $c = 1000$ Ns/m, and $H = 0.8$ m.
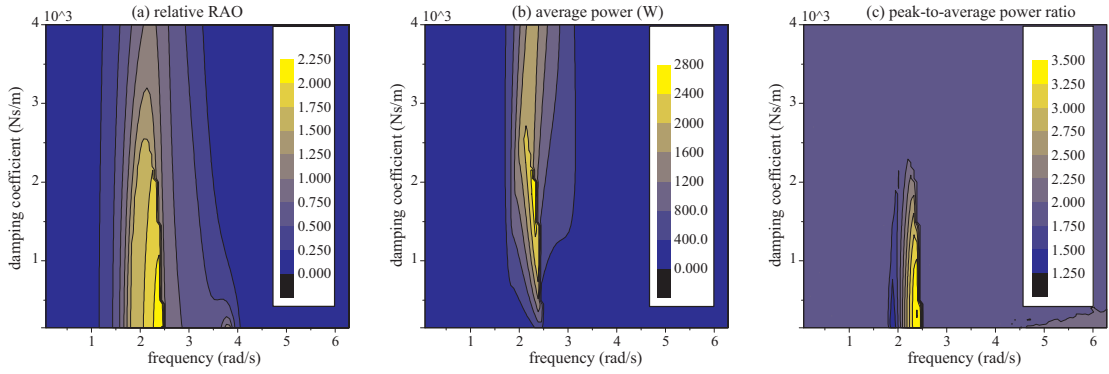

Fig. 8. (a) Relative RAO, (b) average power output, and (c) peak-to-average power ratio, with $c \in [150, 4000]$ Ns/m, $\omega \in [0.06, 6.28]$ rad/s, $M_m = 1500$ kg, $k_1 = 10000$ N/m, $k_2 = 200000$ N/m, $G = 0.6$ m, and $H = 0.8$ m.

4.3 Influence of Gap

Variation in G does not affect the bandwidth of the relative RAO and average power, but has significant influence on their maximum values, as shown in Figs. 7(a)-(b). A small G leads to a small relative RAO and a low average power, since impact events occur periodically and the relative motion is constrained by the impact springs with large stiffness. Consequently, the peak-to-average power ratio is large, mainly due to the low average power output. In contrast to the other design parameters, Fig. 7(c) illustrates that the peak-to-average power ratio is critically sensitive to the variation in G. Therefore, a large G is preferred to achieve a large relative RAO, a high average power and a small peak-to-average power ratio, simultaneously. However, the upper gap limit is bounded by physical constraints, e.g. the buoy height. For this case study, the preferred values are $G \in [0.4, 0.8]$ m.

4.4 Influence of Damping Coefficient

The PTO damping coefficient has a large influence on the dynamics and performance of the vibro-impact WEC, as shown in Fig. 8, where a large damping coefficient results in a small relative RAO and a narrow bandwidth. However, the resonance frequency appears to be unaffected by the PTO damping coefficient. As shown in Fig. 8(b), the average power output is low and the bandwidth is narrow when the damping coefficient is less than 800 Ns/m. The bandwidth appears to be unaffected by the damping

coefficient when it is larger than 1500 Ns/m. Fig. 8(c) also shows that the peak-to-average power ratio tends to small values when the damping coefficient is larger than 1500 Ns/m. Therefore, the preferred damping coefficient values are within $c \in [1500, 2500]$ Ns/m to obtain a large relative RAO, a high average power output, a wide bandwidth, and a low peak-to-average power ratio, simultaneously.

5. CONCLUSION

In this work, a mathematical model of the vibro-impact WEC is derived. Parametric studies are conducted by numerical simulations, which illustrate that the vibro-impact WEC's dynamics and performance, in terms of relative RAO, average power output and peak-to-average power ratio, are sensitive to variations in the design parameters, including the inner mass, spring stiffness, impact gaps and PTO damping coefficient.

Regardless of how these parameters vary, the relative RAO is characterised by a band-pass effect. Hence, the relative RAO is small when the wave frequency is low, indicating high system survivability under extreme sea states, which generally consist of low frequencies. The average power output is sensitive to all the design parameters, while the peak-to-average power ratio seem to be only affected significantly by the impact gap. The bandwidth of the relative RAO and average power output is sensitive to the variations in the inner mass, stiffness of the primary spring, and insensitive to the variations in the stiffness of the impact springs, impact gap, and PTO damping coefficient.

These parametric studies give some basic guidelines for the design of a vibro-impact WEC.

Design optimisation is required to find some sets of the design parameters to achieve a large relative RAO, a high average power output, a wide power capture bandwidth, and a low peak-to-average power ratio. Ongoing work focuses on design optimisation of the proposed vibro-impact WEC to match a specific wave spectrum by panchromatic analysis, and on prototyping of a small scale vibro-impact WEC for wave tank testing.

REFERENCES

Babarit, A. and Delhommeau, G. (2015). Theoretical and numerical aspects of the open source BEM solver NEMOH. In *Proc. EWTEC*, 6–11. Nantes, France.

Babarit, A., Hals, J., Muliawan, M., Kurniawan, A., Moan, T., and Krokstad, J. (2012). Numerical benchmarking study of a selection of wave energy converters. *Renew. Energ.*, 41, 44–63.

Bailey, H. (2010). *Influence of a nonlinear power take off on a wave energy converter*. Ph.D. thesis, The University of Edinburgh.

Chen, W., Dolguntseva, I., Savin, A., Zhang, Y., Li, W., Svensson, O., and Leijon, M. (2017). Numerical modelling of a point-absorbing wave energy converter in irregular and extreme waves. *Appl. Ocean Res.*, 63, 90–105.

Cummins, W. (1962). The impulse response function and ship motions. Technical report, David Taylor Model Basin Washington DC.

Drew, B., Plummer, A., and Sahinkaya, M.N. (2009). A review of wave energy converter technology. *P. I. Mech. Eng. A-J. Pow.*, 223(8), 887–902.

Faedo, N., Peña-Sanchez, Y., and Ringwood, J.V. (2018). Finite-order hydrodynamic model determination for wave energy applications using moment-matching. *Ocean Eng.*, 163, 251–263.

Falcão, A.F.d.O. (2010). Wave energy utilization: A review of the technologies. *Renew. Sust. Energ. Rev.*, 14(3), 899–918.

Falnes, J. (2002). *Ocean waves and oscillating systems: linear interactions including wave-energy extraction*. Cambridge university press.

Fusco, F. and Ringwood, J.V. (2010). Short-term wave forecasting for real-time control of wave energy converters. *IEEE T. Sustain. Energ*, 1(2), 99–106.

Göteman, M., Engström, J., Eriksson, M., Leijon, M., Hann, M., Ransley, E., and Greaves, D. (2015). Wave loads on a point-absorbing wave energy device in extreme waves. In *Proc. ISOPE*. International Society of Offshore and Polar Engineers.

Guo, B., Patton, R., and Jin, S. (2017a). Identification and validation of excitation force for a heaving point absorber wave energy convertor. In *Proc. EWTEC*. Cork, Ireland.

Guo, B., Patton, R., Jin, S., Gilbert, J., and Parsons, D. (2017b). Nonlinear modeling and verification of a heaving point absorber for wave energy conversion. *IEEE T. Sustain. Energ.*, 9(1), 453–461.

Guo, B., Patton, R.J., Jin, S., and Lan, J. (2018). Numerical and experimental studies of excitation force approximation for wave energy conversion. *Renew. Energ*, 125, 877–889.

Guo, B. and Ringwood, J.V. (2020). Modelling of a vibro-impact power take-off mechanism for wave energy systems. In *Proc. ECC*. Saint Petersburg, Russia. Accepted.

Jaya Muliawan, M., Gao, Z., Moan, T., and Babarit, A. (2013). Analysis of a two-body floating wave energy converter with particular focus on the effects of power take-off and mooring systems on energy capture. *J. Offshore Mech. Arct.*, 135(3).

Ricci, P., Lopez, J., Santos, M., Villate, J., Ruiz-Minguela, P., Salcedo, F., and Falcao, A.d.O. (2009). Control strategies for a simple point-absorber connected to a hydraulic power take-off. In *Proc. EWTEC*, 7–10. Uppsala, Sweden.

Ringwood, J.V., Bacelli, G., and Fusco, F. (2014). Energy-maximizing control of wave-energy converters: The development of control system technology to optimize their operation. *IEEE Control Syst. Mag.*, 34(5), 30–55.

Todalshaug, J.H., Ásgeirsson, G.S., Hjálmarsson, E., Maillet, J., Möller, P., Pires, P., Guérinel, M., and Lopes, M. (2016). Tank testing of an inherently phase-controlled wave energy converter. *Int. J. Mar. Energy*, 15, 68–84.

Zhan, S. and Li, G. (2018). Linear optimal noncausal control of wave energy converters. *IEEE T. Contr. Syst. T.*, 27(4), 1526–1536.

Zhang, X., Yang, J., and Xiao, L. (2014). Numerical study of an oscillating wave energy converter with nonlinear snap-through power-take-off systems in regular waves. *J. Ocean Wind Energy*, 1(4), 225–230.

Appendix A. PARAMETERS

Simulation conditions are: buoy radius $r = 1$ m, height $h = 2$ m, draft $d = 1$ m, total mass of the buoy and inner mass $M_t = M_b + M_m = 3,220.13$ kg, water density $\rho = 1,025$ kg/m^3, gravity constant $g = 9.81$ N/kg, added mass at infinite frequency $m_\infty = 1,883.47$ kg, and wave height $H = 0.8$ m.

The system matrices in Eqs. (4) and (5) are

$$A_r = \begin{bmatrix} -1.50, -2.06, 1.54, -0.35 \\ 2.06, -0.01, 0.07, -0.02 \\ -1.54, 0.07, -2.38, 1.96 \\ -0.35, 0.02, -1.96, -0.54 \end{bmatrix},$$

$$B_r = \begin{bmatrix} -403.88, 22.57, -181.05, -49.82 \end{bmatrix}^T,$$

$$C_r = \begin{bmatrix} -4.04, -0.23, 1.81, -0.50 \end{bmatrix}.$$

The system matrices in Eqs. (10) and (11) are

$$A_e = \begin{bmatrix} -0.05, -0.61, -0.13, -0.24, -0.13, -0.12 \\ 0.61, -0.19, -1.13, -0.29, -0.39, -0.24 \\ -0.13, 1.13, -0.39, -1.56, -0.47, -0.52 \\ 0.24, -0.29, 1.56, -0.62, -2.04, -0.66 \\ -0.13, 0.39, -0.47, 2.04, -0.88, -2.38 \\ 0.12, -0.24, 0.52, -0.66, 2.38, -1.21 \end{bmatrix},$$

$$B_e = \begin{bmatrix} -549.4, 884.3, -1008.7, 939.5, -784.6, 603.3 \end{bmatrix}^T,$$

$$C_e = \begin{bmatrix} -5.49, -8.84, -10.09, -9.39, -7.85, -6.03 \end{bmatrix},$$

$$D_e = \begin{bmatrix} 49.85 \end{bmatrix}.$$